Geophysical Research Letters

Supporting Information for

Solving a Seismic Mystery with a Diver's Camera: A Case of Shallow Water T-waves in the Persian Gulf

Amir Salaree, Zack Spica and Yihe Huang

University of Michigan, Ann Arbor, MI, USA

Contents of this file

- Sections S1 to S15
- Figures S1 to S20
- Equations S1 and S3

Introduction

The supporting information includes 15 sections:

S1 Iranian Seismic Networks

S2 The Kish/Charak Cluster

S3 CCTV Footage of the Kish Island Earthquake

S4 SCARDEC Source Time Function of the 25 June 2022 Kish Island Earthquake

S5 Slowness Parameter of the 2022 Earthquake Sequence in Southern Iran

S6 Location Uncertainty of the 25 June 2022 Kish Island Earthquake

S7 The Fish's Response to the Acoustic Signal

S8 Details of the Acoustic Propagation Model

S9 Persian Gulf Bathymetry

S10 Acoustic Propagation on Slopes

S11 Computation of $\tau_{1/3}$ for the Kish Island Earthquake

S12 Iranian Strong Motion Data

S13 Sonifying the Acoustic Propagation

S14 Seismic Response of the Kish Island

S15 Deployment of New Instruments in the Persian Gulf

The supporting information includes 20 figures:

Figure S1 is a map of the Iranian seismic networks.

Figure S2 shows the distribution of azimuthal gaps for synthetic offshore events using existing current stations.

Figure S3 illustrates the migration of the Charak cluster events over time.

Figure S4 is a snapshot of a CCTV footage of the shaking from the Kish Island earthquake.

Figure S5 shows the time series and Fourier transform of the audio track from supplementary video SV2.

Figure S6 shows the SCARDEC source time function of the Kish earthquake.

Figure S7 is a rendition of slowness parameter for the Kish earthquake in the M_0-E^E space.

Figure S8 shows the relocation setup for the Kish earthquake.

Figure S9 depicts the P-wave arrivals at the IRSC stations for the Kish earthquake.

Figure S10 is a snapshot of motion tracking of the fish in the divers' video.

Figure S11 shows our model schematics for acoustic propagation.

Figure S12 illustrates the variations in frequency and group velocity from changes in model parameters.

Figure S13 shows depth and slope distribution in the Persian Gulf.

Figure S14 is a set of snapshots from acoustic propagations in flat, uphill and downhill systems.

Figure S15 is a global map of stations used on the computation of $\tau_{1/3}$.

Figure S16 shows available strong motion records of the $M_L = 5.6$ Kish earthquake from BHRC stations.

Figure S17 depicts the spectral response of the Kish Island as a rectangular basin.

Figure S18 is a seismicity map of the Persian Gulf region.

Figure S19 is a map of submarine telecommunication cables in the Persian Gulf.

Figure S20 show the proposed locations of a network of HBox stations in the Persian Gulf.

S1 Iranian Seismic Networks

Several seismic networks exist in Iran each of which are operated by separate agencies. Among these the major two networks are maintained by the Iranian Seismological Center (IRSC) and the International Institute of Earthquake Engineering and Seismology (IIEES). The IRSC network with the largest number of stations in Iran is comprised of both short-period and broadband instrument. The IIEES, however, operates a network of only broadband stations. Fig. S1 shows the distribution of stations in both networks where Kish Island is marked by a white arrow.

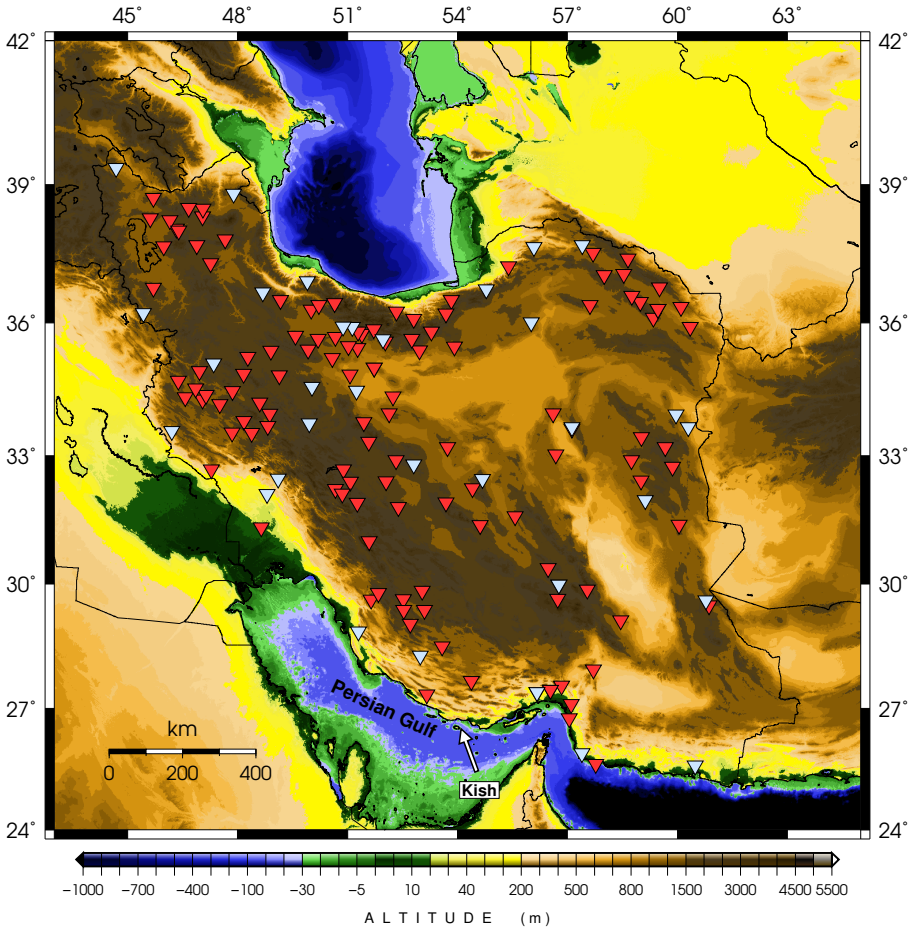

Figure S1: The two major Iranian seismic networks. Red and blue triangles show stations operated by the Iranian Seismological Center (IRSC) and the International Institute of Earthquake Engineering and Seismology (IIEES), respectively.

S1.1 Offshore Azimuthal Gap in the Persian Gulf

The geographic position of the Persian Gulf at the south of Iran and the lack of offshore instrumentation due to the shallow bathymetry has resulted in a lopsided distribution of seismic stations. This leads to large azimuthal gaps for offshore events as demonstrated in Fig. S2. In Fig. S2, the azimuthal gaps are computed for hypothetical offshore events as nodes of a 2-km resolution grid. The events grid is designed to cover the geographic span of recorded seismicity in the IRSC catalog (shown as black dots).

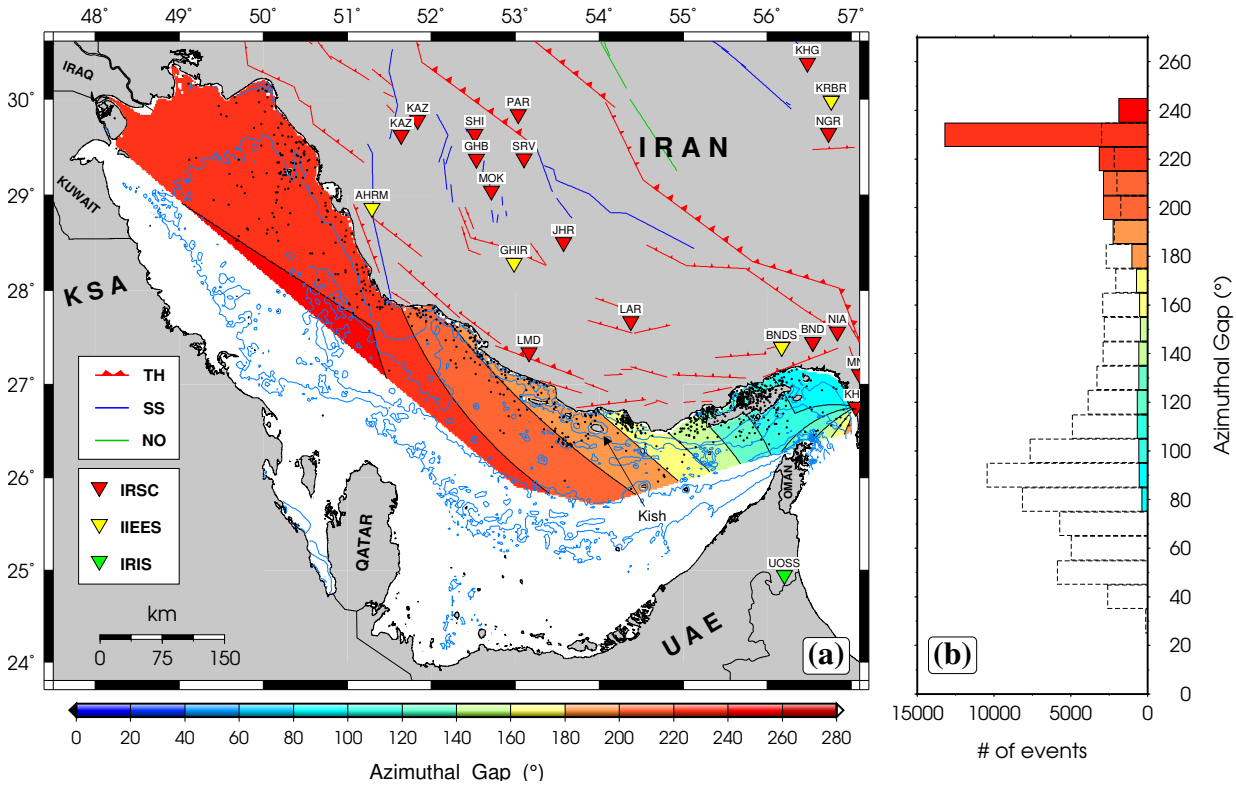

Figure S2: (a) Azimuthal gaps for offshore earthquake scenarios in the Persian Gulf designed as nodes of a 2-km resolution grid, using the existing stations in the region. Stations are colored based on their respective operating agencies. Fault traces and their mechanisms (TH: thrust, SS: strike-slip, NO: normal) are also shown (Hessami et al., 2003). Black dots are offshore earthquakes from the IRSC catalog. Blue contours represent bathymetry (GEBCO, 2021). Kish Island is marked by a black arrow. (b) Distribution of offshore azimuthal gaps from (a). Dashed bars show the onland azimuthal gaps using the same stations.

S2 The Kish/Charak Cluster

A cluster of 147 small to moderate size earthquakes with a largest $M_L \leq 5.6$ event shook the Port of Charak in Southern Iran between June 14 and September 14, 2022. The seismicity started near Charak and gradually moved outwards within a 30 km radius, with the larger events occurring offshore in the south. The largest earthquake in the series, an $M_L = 5.6$

The cluster was the first part of a larger sequence in southern Iran and was followed by two other clusters: (1) 24 events near Parsian, $\sim$ 120 km west of Charak during June 21-22 ($M_L \leq 5.2$), and (2) 172 events near Port of Khamir, $\sim$ 120 km east of the first cluster during July 1 to September 19 ($M_L \leq 6.1$), according to the IRSC catalog (supplementary video SV1). The entire sequence caused considerable shaking in the eastern Persian Gulf region and resulted in numerous landslides and rockfalls near Ports of Charak and Khamir reaching peak ground acceleration values of 229 cm/s^2 and 96 cm/s^2, respectively (BHRC, 2023). The $M_L = 6.1$ doublet on July 1 in the latter cluster incurred significant damage to the Port of Khamir and demolished several villages.

The sequence seems to have taken place on a major basement thrust system called the Zagros Foredeep Fault, which merges in the north into the Mountain Front Fault as shown in Fig. 1a; MFF marks the northeastern edge of the coastal plain of the Persian Gulf (Nissen et al., 2011). These fold and thrust systems are results of Eurasia-Arabia convergence the strain from which is either released in the form of small to moderate earthquakes like the 2022 sequence, or deformation via active décollement (Berberian, 1995). Most of the seismicity in the area is shallow with a USGS median depth of 17 km. The almost nonexisting disconformities in the Arabian shield towards the Persian Gulf (Jong, 1982) have resulted in the notable lack of recorded seismicity and, thus almost the entire seismic activity takes place in the north.

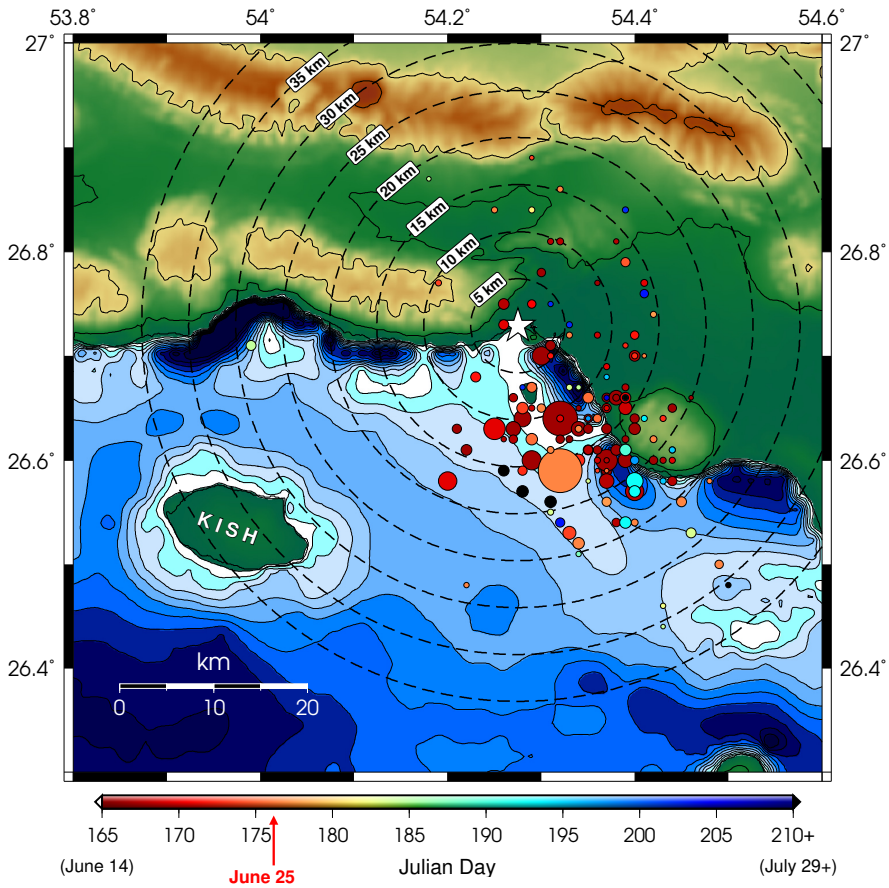

Figure S3: Earthquakes of the 2022 Kish cluster shown as circles color-coded according to their Julian days. Circle sizes are proportional to earthquake magnitude with the largest, $M_w = 5.6$ occurring on 25 June 2022. Dashed circles show distance from the first event in the cluster, depicted by a white star.

S3 CCTV Footage of the Kish Island Earthquake

The near-field shaking from the 25 June 2022 $M_L = 5.6$ earthquake was recorded in the CCTV footage across the Kish Island. Fig. S4 shows a snapshot of an example of such videos recorded at a clothing store (see supplementary video SV2).

Figure S4: Snapshot form the beginning of the CCTV footage from a clothing shop in the Kish Island showing the shaking from earthquake.

The analysis of the audio track from the video shows a 10 s long signal starting at approximately 07:07:18.5 (Fig. S5). The starting time matches the near-field arrival of a wave train from the earthquake (origin time 03:37:13 GMT or 07:07:13 IRST) at a $\sim$ 34 km distance (using the $t_S - t_P \sim 4$ s from Fig. S5, a Poissonian crust, and a relatively shallow raypath with $V_S = 3.5$ km/s). One can consider the shelved items in the shop in Fig. S4 as damped oscillators. As such, the very low amplitude (due to small source) and the

comparatively moderate large to moderate returning forces (gravity and friction) result in an over-damped system (Aki & Richards, 2002). Therefore, the duration of observed shaking would approximately correspond to the duration of incoming wave train.

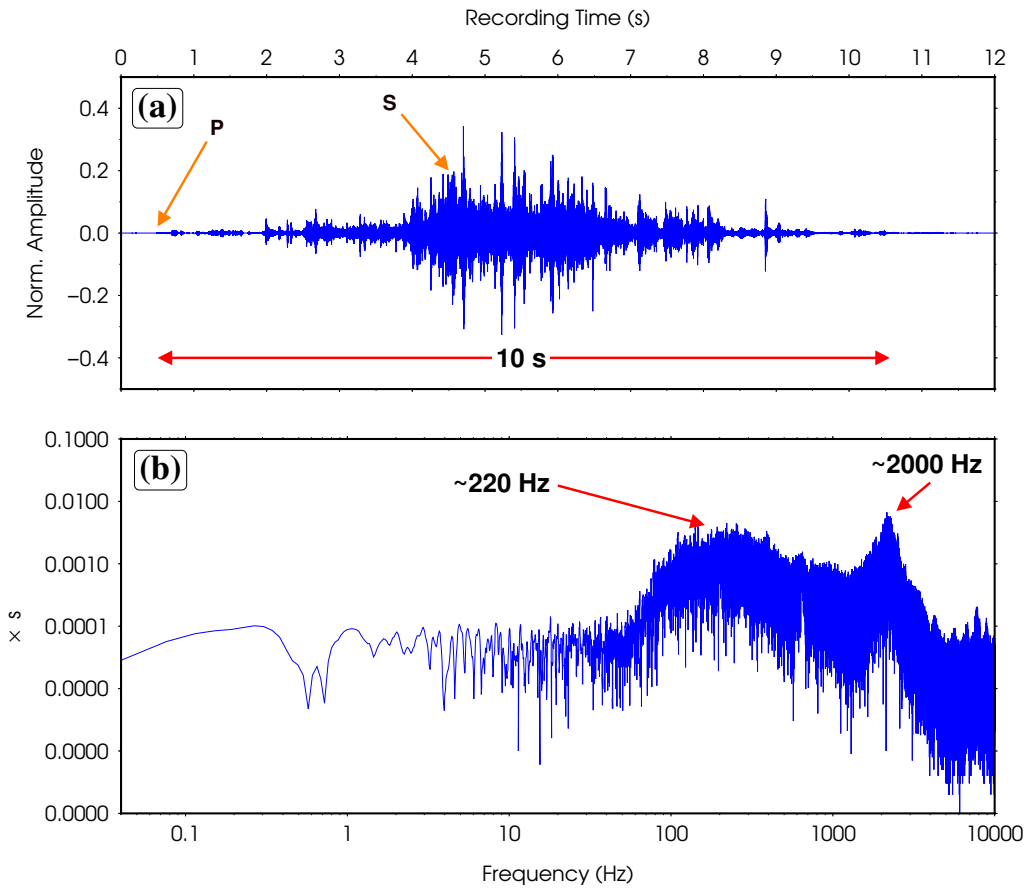

Figure S5: (a) The time series from the audio track of the recording at the clothing shop (Fig. S4 in supplementary video SV2. **(b)** Frequency content of the record shown in (a). The two dominant frequencies are marked by red arrows.

S4 SCARDEC Source Time Function of the 25 June 2022 Kish Island Earthquake

Fig. S6 shows the SCARDEC (Vallée et al., 2011) source time function of the 25 June 2022 $M_L = 5.6$ Kish Island earthquake

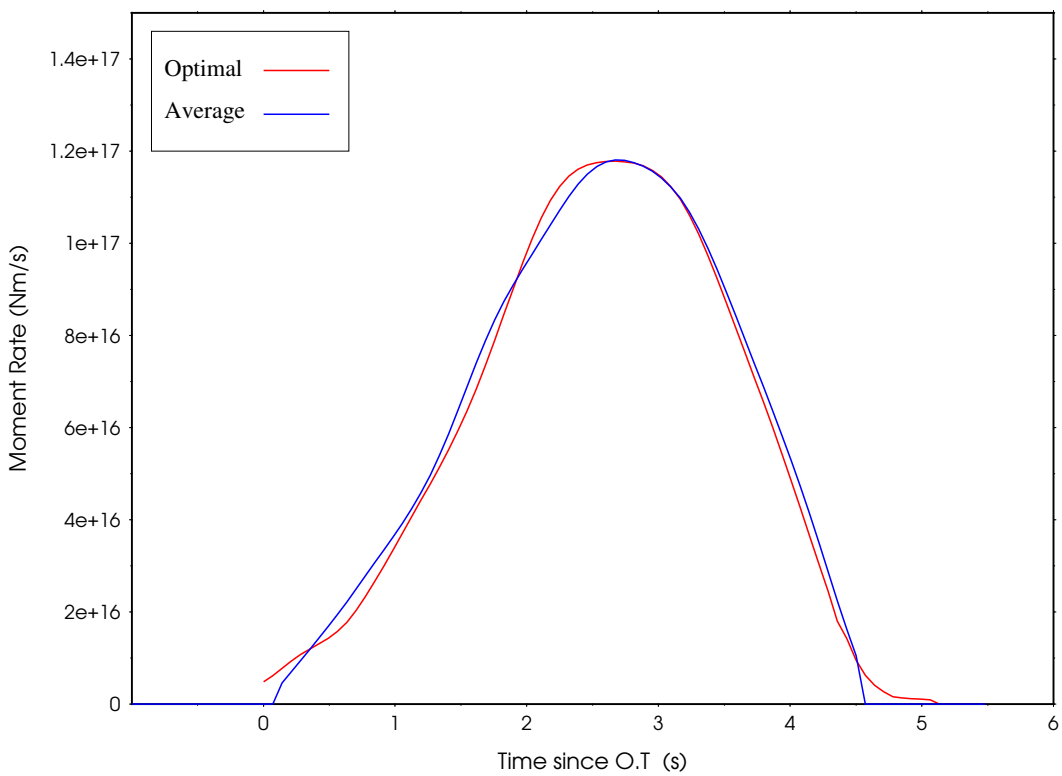

Figure S6: SCARDEC source time function of the Kish Island earthquake (personal comm. Martin Valée)

S5 Slowness Parameter of the 2022 Earthquake Sequence in Southern Iran

In their effort to formalize rupture slowness using earthquake scaling laws, Newman & Okal (1998) introduced the slowness parameter Θ as the ratio of estimated radiated energy, E^E from the source to its seismic moment, M_0, or

$$\Theta = \log_{10} \frac{E^E}{M_0} \tag{S1}$$

In this formalism, E^E is calculated using only the teleseismic ($35° \leq \Delta \leq 80°$) body waves and typically no information regarding source mechanism or the focal depth are needed. The distance range is selected to avoid complexities in the waveforms caused by shallow and deep Earth structures, respectively appearing in the form of seismic triplication and diffusion/scattering from the core. Slowness parameter is expected to be a constant, i.e., $\Theta = -4.9$ for all earthquakes, but there can be some variations within the range of $-7.0 \lesssim \Theta \lesssim -3.0$ where the low and high bounds represent slow and fast ruptures, respectively. In this regard, fast or "snappy" ruptures exhibiting slowness values higher than $\Theta = -4.9$ and towards $\Theta = -3.0$ have higher frequency content and often result in more apparent shaking, hence demonstrating higher PGA.

Computations of Θ for $M_w \geq 5.0$ in the 2022 Iranian sequence reveals a relatively strong snappy flavor to these events as shown in Fig. S7. This result is in agreement with the documented strong shaking both in Iran and in the southern Persian Gulf. The choice of magnitude threshold was made empirically as a cut-off limit where the teleseismic signal-to-noise ratio becomes too low at GSN stations, resulting in unrealistically high slowness values.

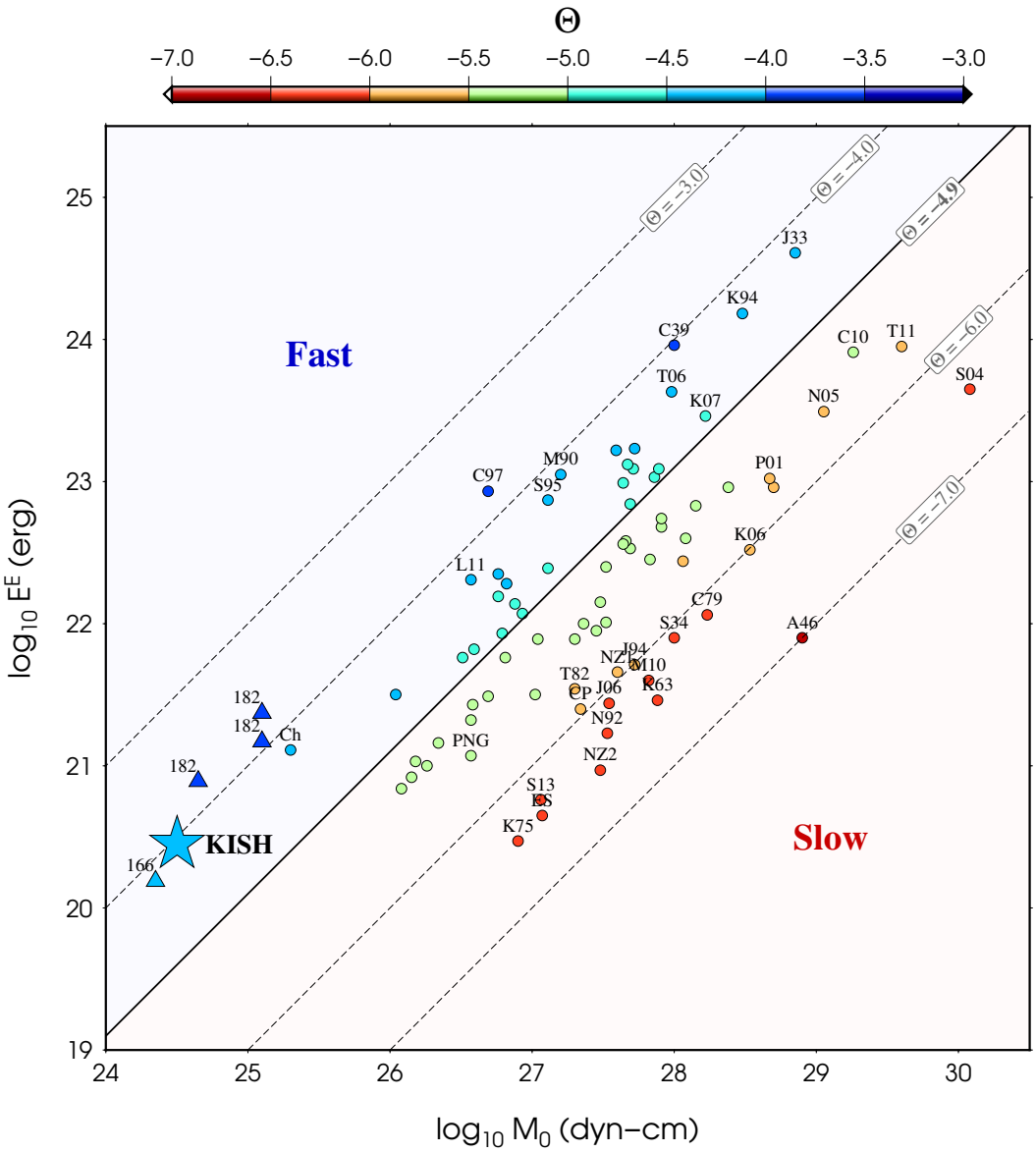

Figure S7: Slowness parameter from the 2022 Iranian sequence shown as triangles on a background of Θ values for other earthquakes in the world. The Kish Island earthquake is depicted by a star. Earthquakes are color-coded based on their slowness value.

S6 Location Uncertainty of the 25 June 2022 Kish Island Earthquake

In an effort to reconcile the location disparity associated with the $M_L = 5.6$ Kish earthquake, we relocated the IRSC and ISC epicenters using the available phase data from the respective agencies. The relocation process was carried out using the iterative algorithm by Wysession et al. (1991). Relocation of the IRSC epicenter moves it by ~ 10 km to the west, albeit with considerable uncertainty, depicted by the computed red ellipse in Figs. S8 and 1a. The uncertainty arises from the sparse local network (see section S1) as well as inconsistencies in the reported arrival times, as shown in Fig. S9. These inconsistencies (sometimes > 10 s) at IRSC stations occur at various distances are of unknown origin. Relocation of the ISC epicenter, however, does not move the published epicenter. The relocation result has very small uncertainty shown with the small black ellipse.

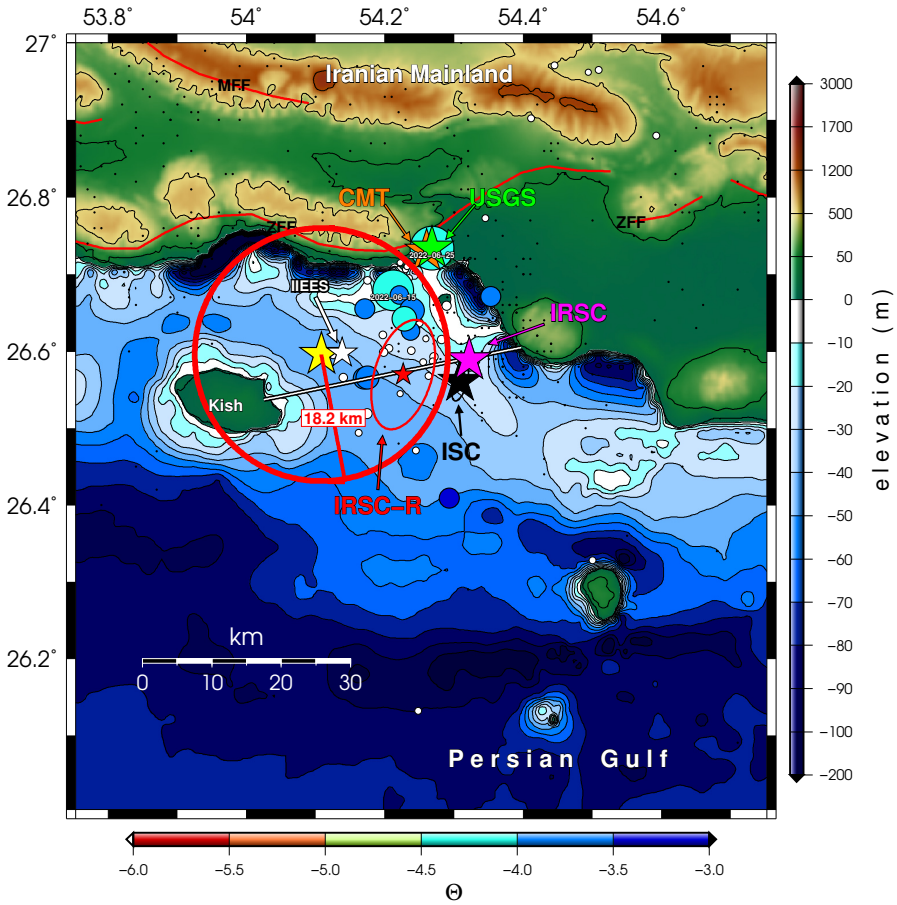

Figure S8: Published locations for the $M_L = 5.6$ earthquake near Kish Island on 25 June 2022. Pink, black, white, green, and orange stars depict the epicenters published by IRSC, ISC, IIEES, USGS, and CMT, respectively. Red star represents the relocated IRSC epicenter using the available phase data, and red (IRSC-R) and black ellipses show the relocation uncertainties. Position of divers is marked by a yellow star. The red circle shows the computed epicentral distance at the location of divers obtained from the video recording. Circles are earthquakes in the cluster colored according to their corresponding slowness value; small, white circles depict small events for which no slowness was calculated. Black dots represent historical seismicity. Red lines show fault lines.

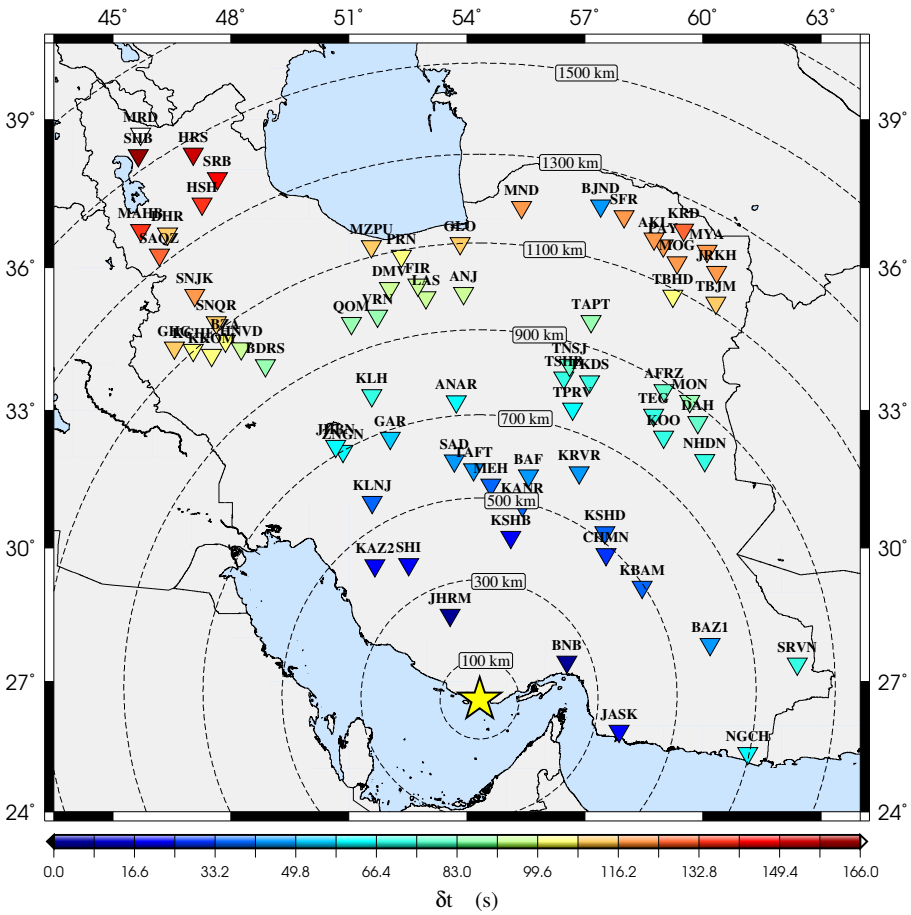

Figure S9: P-wave arrivals at the IRSC stations shown by triangles (`www.irsc.ut.ac.ir`; accessed on 4 Aug. 2022). Circles represent distance from the epicenter shown as a yellow star.

S7 The Fish's Response to the Acoustic Signal

Indifference of the fish in the divers' video can be used as a proxy to the recorded signal. We note that based on the shallow water approximation (considering that in the Persian Gulf $H << W$ with H and W as sea depth and fault width) the vertical gradient of horizontal motion is practically zero and the squall-like motion of the water column will inevitably displace the floating material at the sea bed (Synolakis, 1999). Thus a nonexisting uniform, continuous component of motion among the fish with a celerity matching that of a gravity wave at the site ($c = \sqrt{g\,h} \sim 20$ m/s) points to a non-gravity wave, hence ruling out the possibility of a tsunami.

To investigate, we analyzed the motion of a group of small, white fish compared to the motion of a larger, striped fish by means of motion tracking 1.3 s of the divers' video during the sixth boom (B6), as shown in Fig. S10. We have used the relative location vector of the four small fish with respect to the larger fish (in turn measured from a fixed point on the hollow jar) over time a a measure of the fish's motion. The resultant displacement vector, $\vec{D}$ thus represents the overall motion of the shoal of fish. Our analysis of the results reveals that the changes in the normalized displacement vector, i.e., $|\vec{D}|/|\vec{D_0}|$ over the selected time window are not significant ($< 30\%$). Supplementary video SV4 shows the measured changes over time during the selected window. The observed change in the vector seems to have occurred smoothly during the diver's approach, as can be seen in Fig. S10b. Based on this result, we determine the signal to be of acoustic nature.

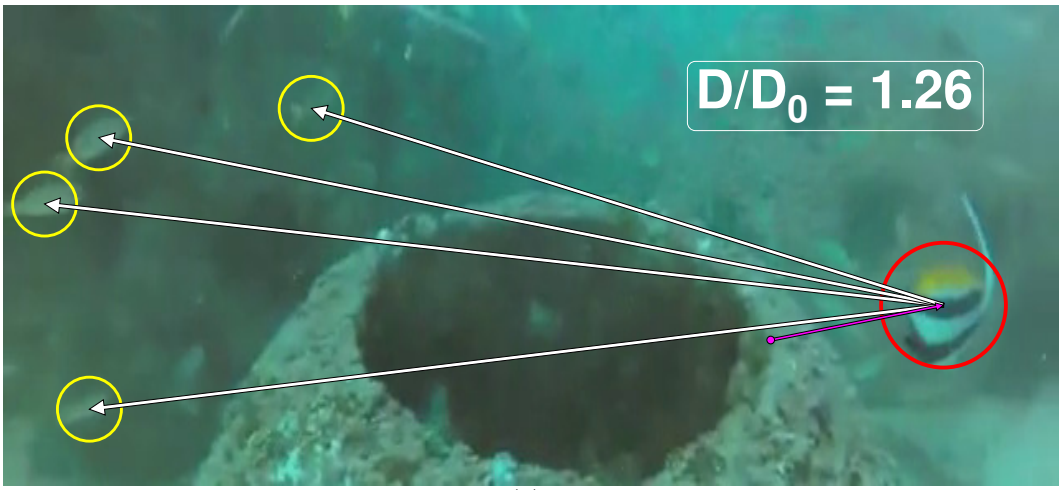

(a)

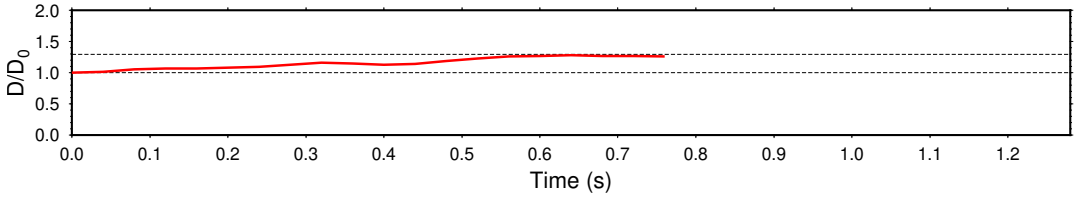

(b)

Figure S10: (a) Motion tracking snapshot of the fish in the divers' recording. The pink arrow represents absolute position of the larger, striped fish with the corner of the hollow jar as reference. White arrows show relative positions of the smaller, white fish compared to the striped fish. (b) Progress of the D/D_0 parameter over video's lengths.

On the high frequency end, the fish's indifference to the signal and the lack of erratic motions among them alludes to a signal with a dominant frequency smaller than $f = 100$ Hz and significantly less than $f = 1000$ Hz. This is because the auditory response of the fish usually either peaks or only exists at frequencies larger than $f > 100$ Hz Nedwell et al. (2004), while it is most efficient at $f \sim 1000$ Hz. This is in agreement with the dominant measured dominant frequency of $f \sim 45$ Hz shown in Fig. 2.

S8 Details of the Acoustic Propagation Model

We model the acoustic propagation from a seismic source as a monochromatic ray from the elastic-to-acoustic conversion point toward the receiver, bouncing up and down between the seabed and the free surface. In this formalism, the conversion point belongs to a seismic ray arriving at a take-off angle, i_0 from a hypocenter placed at a depth of H as shown in Fig. S11. The point source (yellow star in Fig. S11) in this setup is a representative of an impulsive source as a good approximation for a small-to-moderate event. D is the horizontal moveout from the take-off angle. In Fig. S11, v_a, v_P, and w are the acoustic velocity of water, elastic P wave velocity in the sea bed, and depth of the water column. Note that v_a is different from v_g which is computed as the apparent group velocity of propagation. The dominant frequency is the inverse weighted integral of reflection intervals; equivalent to the average of point frequencies along the path.

$$f = \frac{v_a}{w}\sqrt{1 - \frac{v_a^2}{v_P^2}\frac{\tan^2 i_0}{(1+\tan^2 i_0)}} \qquad , \qquad v_g = v_a\sqrt{1-(v_a/v_P)^2\sin^2 i_0} \tag{S2}$$

We have not included attenuation in this model. Obviously, this simple model requires modifications in the presence of inclined sea bed and irregular bathymetry. However, under such circumstances the problem can be solved numerically.

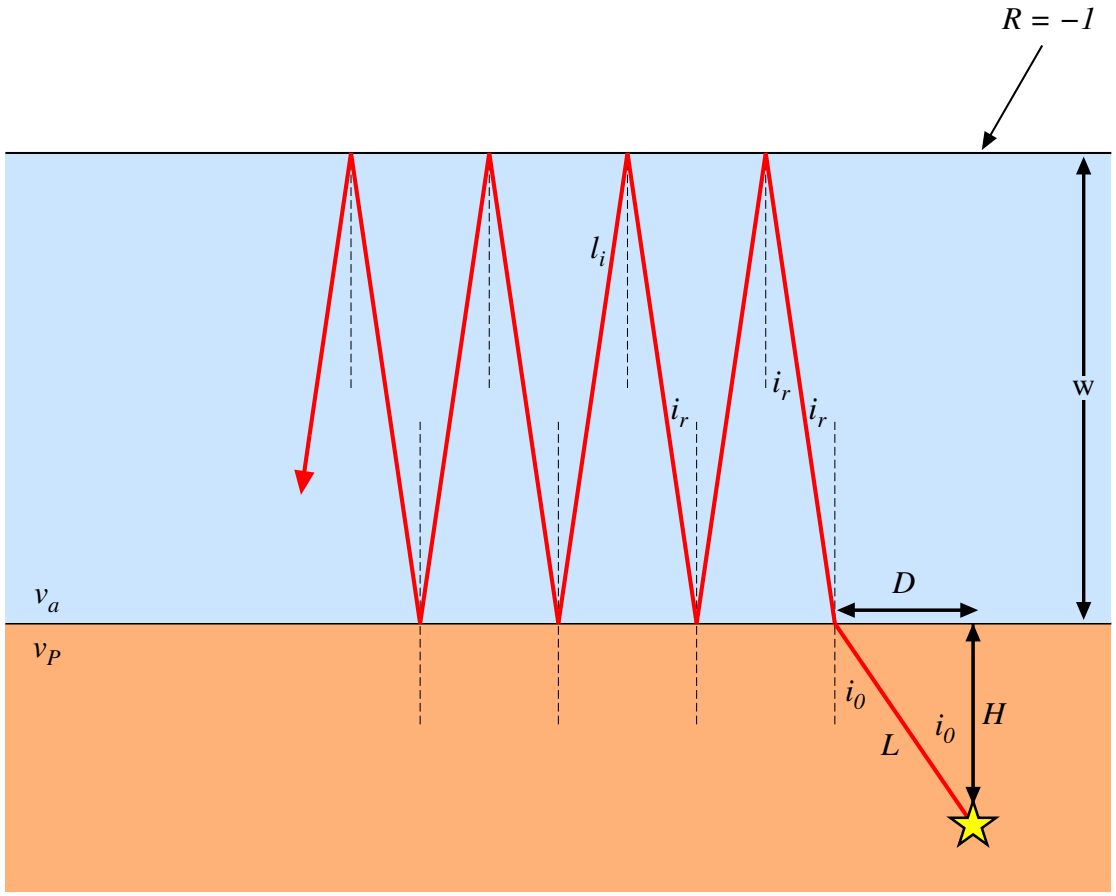

Figure S11: Schematics of the acoustic generation and propagation model. The star represents an arbitrary point in the source, at the depth of H. R and w, v_a, and v_P are reflection coefficient, water depth, acoustic velocity, and the velocity of P/S waves respectively.

Fig. S12 shows the variations in frequency and group velocity from changes in model parameters (see Eq. (S2)). White dots in the left panel of Fig. S12 mark the frequency range of our interest from the divers' video. The dots in the right panel of Fig. S12 correspond to their counterparts in the left panel.

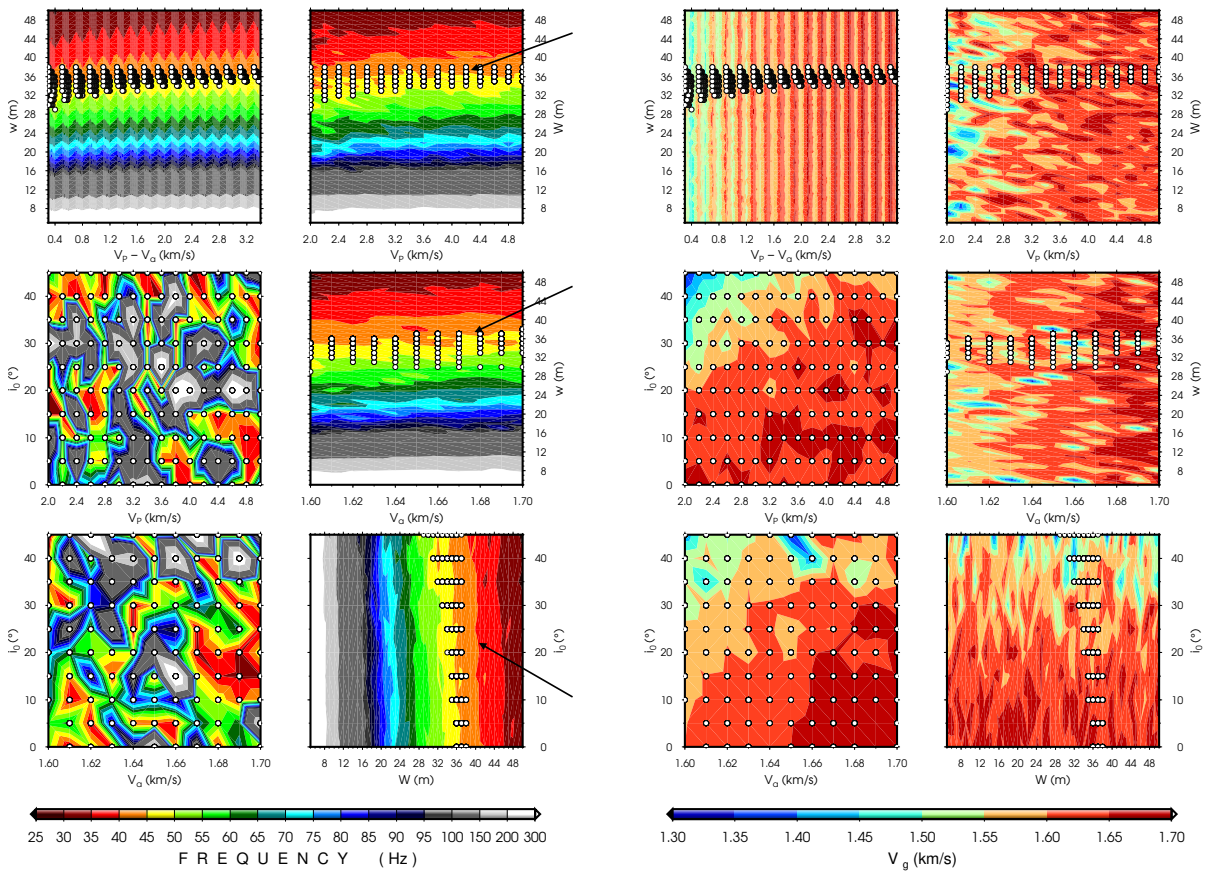

Figure S12: Variations in *(left)* frequency and *(right)* following different permutations of water depth (w), elastic velocity (v_P), acoustic velocity (v_a), velocity gradient at the conversion boundary ($v_P - v_a$), and take-off angle (i_0). White dots mark the values for which frequency is $f = 45 \pm 1$ Hz, also marked by black arrows on the left panels.

S9 Persian Gulf Bathymetry

Bathymetry and slope maps of the Persian Gulf are shown in Fig. S13.

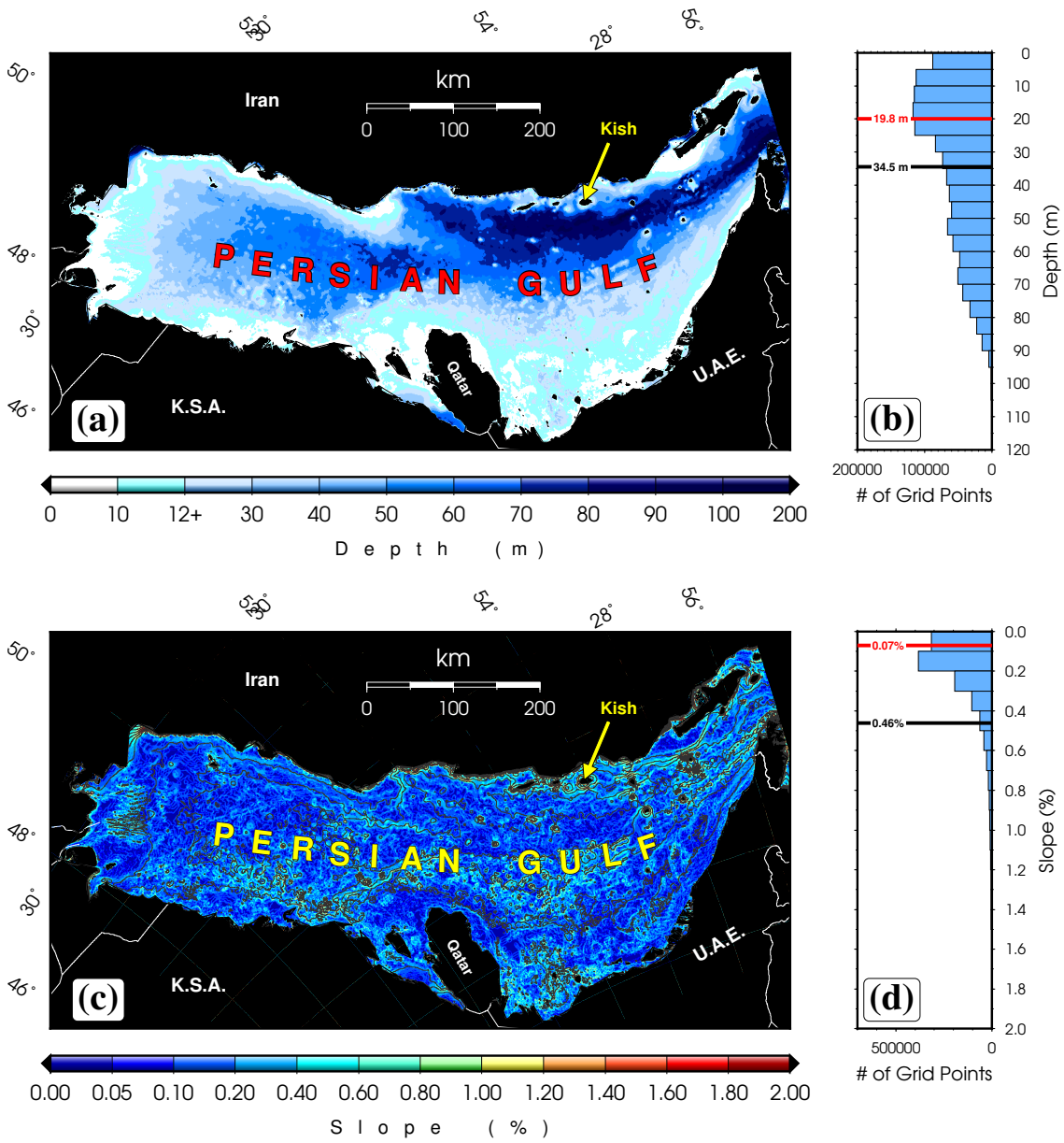

Figure S13: (a) Bathymetry of the Persian Gulf. (b) Depth histogram of the GEBCO grid. (c) Slope distribution in percent calculated as the modulus of the gradient field of bathymetry in (a). (d) Slope histogram of GEBCO. The Kish Island is marked by a yellow arrow in (a) and (c). Median and mean of depth and slope are shown respectively by red and black lines in (b) and (d).

S10 Acoustic Propagation on Slopes

Numerical solution of the acoustic propagation in a flat sea bed as prescribed by our simple model (Eq. (S2)) is shown in Fig. S11 (note that the horizontal and vertical axes in Fig. S14 are plotted on different scales). In the presence of inclined bathymetry, however, the propagation is more complex. In the downhill direction (Fig. S14b) the incidence angles will increase upon each reflection (by twice the slope angle as shown by Johnson et al. (1963)) and as a result the apparent group velocity also increases. The fewer vertical propagation results in a decrease in acoustic frequency (note the variation in audio frequency in the supplementary video SV4). The situation is reversed for the case of uphill propagation. In this scenario the incidence angle progressively decreases until the propagation either comes to a full stop or flips direction (Fig. S14c), depending on the boundary conditions. For abyssal phases, i.e., acoustic signals converted or propagating in bathymetric local minima, this may result in stagnant phases whereby the wavefront keeps going back and forth on a small scale.

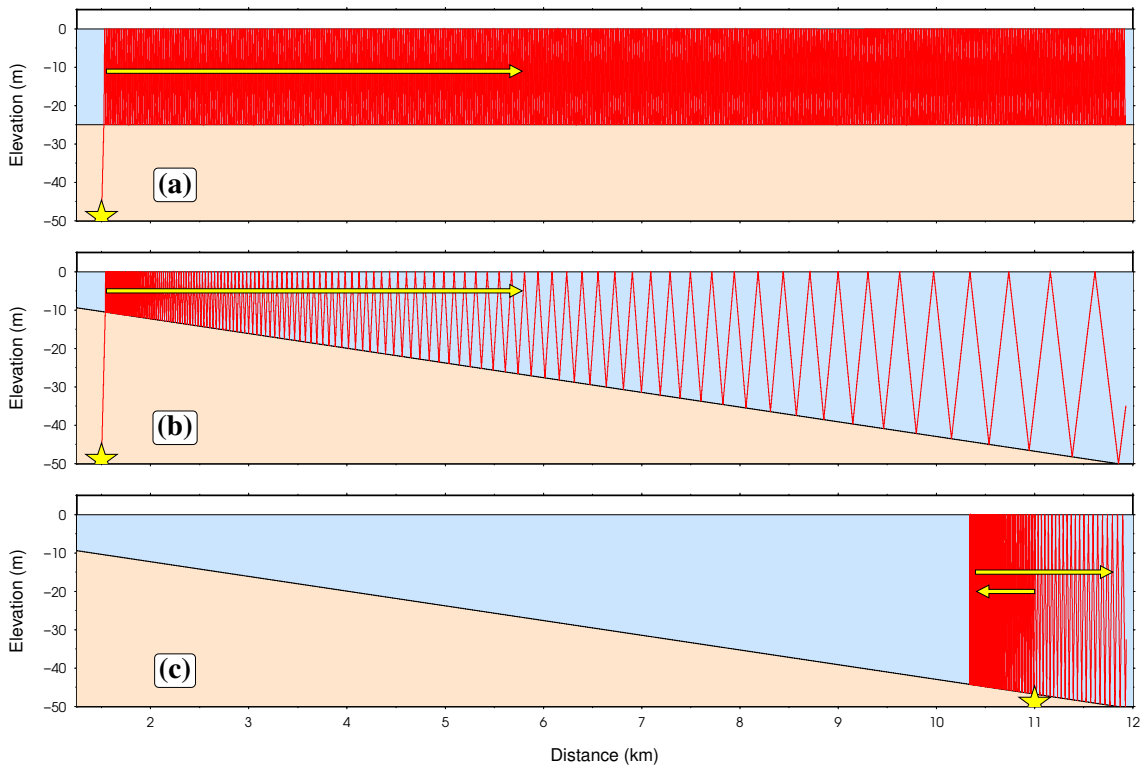

Figure S14: Propagation of acoustic rays on (a) flat seabed, (b) downhill, and (c) uphill directions. Seabed and water are shown in beige and blue. Earthquake locations (exaggerated depth) are depicted by yellow stars. Horizontal and vertical axes' units are in kilometers and meter, respectively. Yellow arrows show propagation direction.

S11 Computation of $\tau_{1/3}$ for the Kish Island Earthquake

Fig. S15 shows the teleseismic stations used in the $tau_{1/3}$ algorithm.

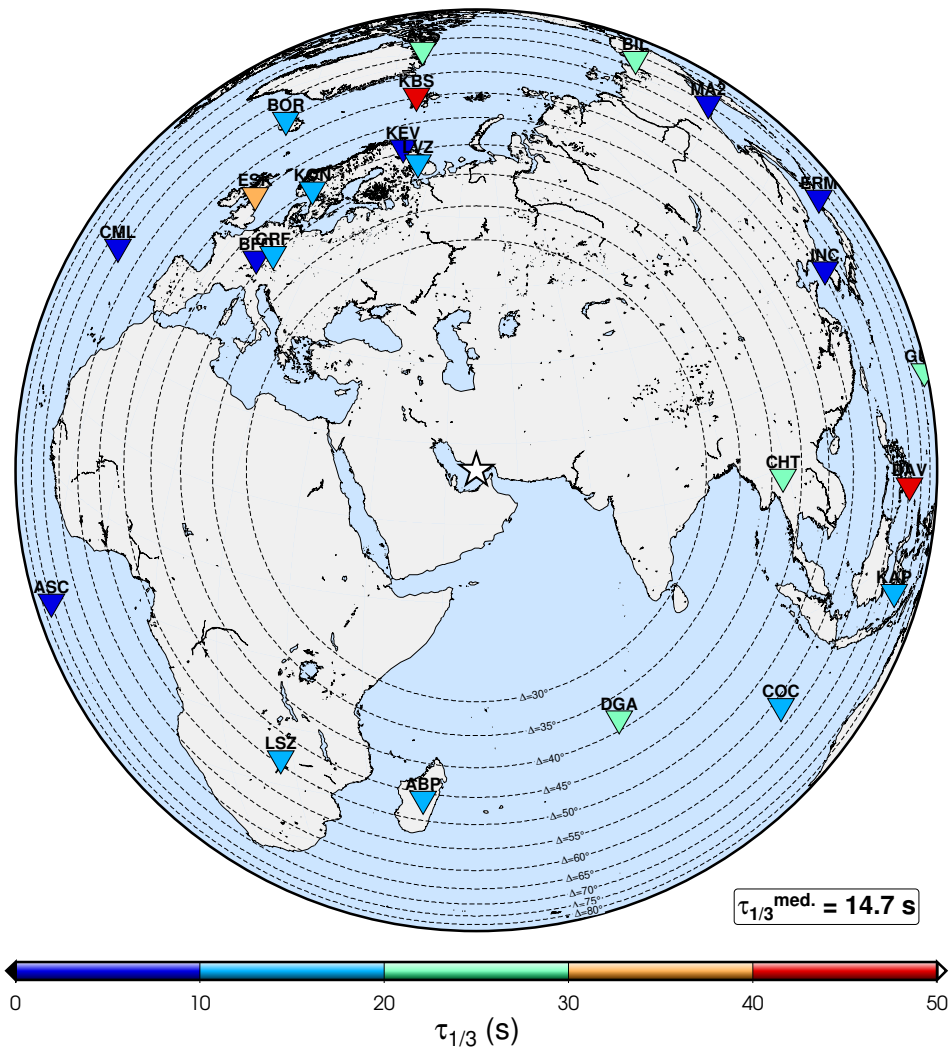

Figure S15: Global distribution of earthquakes used in the computation of $\tau_{1/3}$. Stations are color-coded based on their respective values of $\tau_{1/3}$. The median $\tau_{1/3} = 14.7$ s is also shown. Epicenter of the Kish Island earthquake is marked by a white star.

S12 Iranian Strong Motion Data

Fig. S16 shows the available strong motion records of the 25 June 2022, $M_L = 5.6$ Kish earthquake from the Iranian BHRC network.

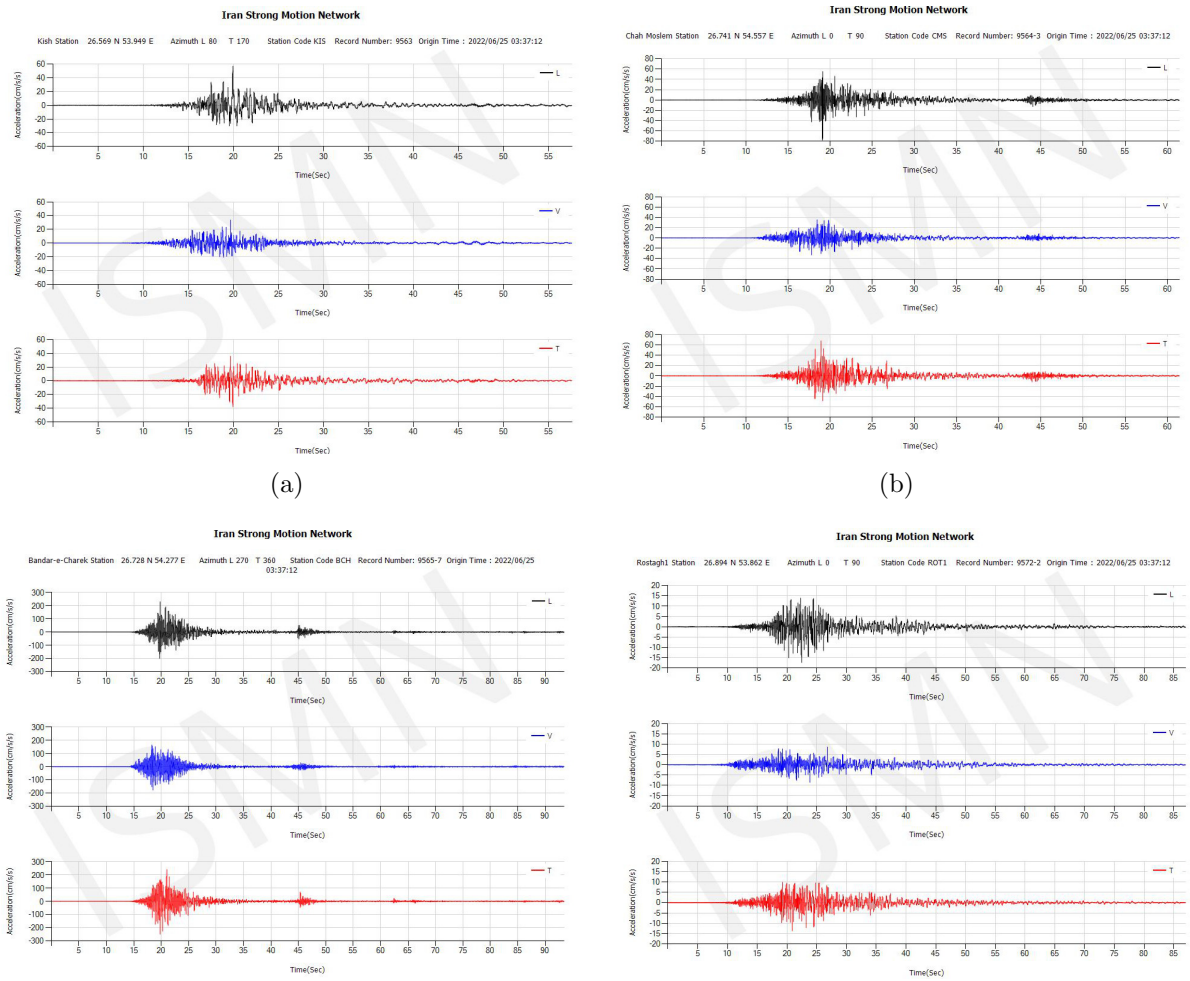

(a) (b) (c) (d)

Figure S16: Strong motion records from BHRC for the 25 June 2022 Kish earthquake.

S13 Sonifying the Acoustic Propagation

In order to demonstrate the variations in the frequency content of acoustic signals along the path, one can turn the reflection times at the sea bed and surface into time series of "audio blips" modulated on a high-frequency carrier sine wave. The result is shown for the propagation in Fig. 3 as the supplementary video SV5.

S14 Seismic Response of the Kish Island

A first order spectral response can be computed for the Kish Island by approximating the total island relief as a uniform rectangle. Such a simple model is supported by previous studies of the structural properties and geographic shape of the island (e.g., Ataie-Ashtiani et al., 2013). Thus, we compute the natural response of the rectangular ($a \times b$) Kish Island as a modal function of its overtones (see Salaree & Huang, 2023):

$$f_{m,n} = \frac{0.5 \times v_S}{\sqrt{(\frac{m}{a})^2 + (\frac{n}{b})^2}} \tag{S3}$$

where v_S is shear wave velocity, and a and b are overtone multipliers along the sides of the rectangle. Fig. S17 shows the two lowest computed natural frequencies (primary $f_{1,1}$ and the first overtone $f_{1,2}$) a functions of shear wave velocity for $a = 14$ and $b = 7.5$ km in Eq. (S3).

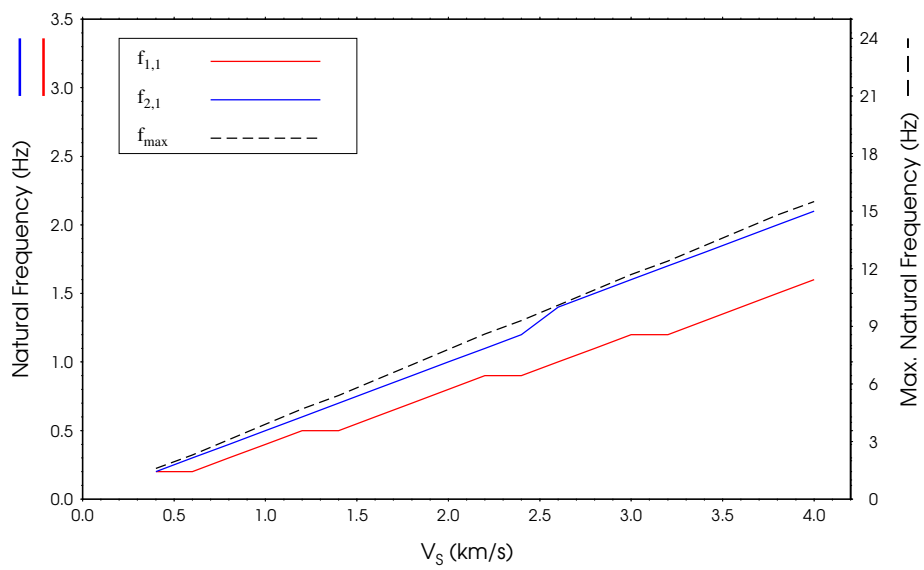

Figure S17: Spectral response of the Kish Island as a rectangular basin as a function of shear wave velocity. Red and blue curves are first and second modes. The dashed black line shows the maximum frequency (highest overtone) plotted on a different scale (to the right).

S15 Deployment of New Instruments in the Persian Gulf

Nearly all the seismicity of the Persian Gulf is concentrated along its northern margins, i.e., the Iranian coastlines as shown in Fig. S18. Consequently, any effort to mitigate the seismic and tsunami hazard from these earthquakes and near-field early warning must be concentrated along these shorelines. We note that the strong far-field shaking along the southern shorelines from the the acoustic waves as described in the main text occurs after significant time lags.

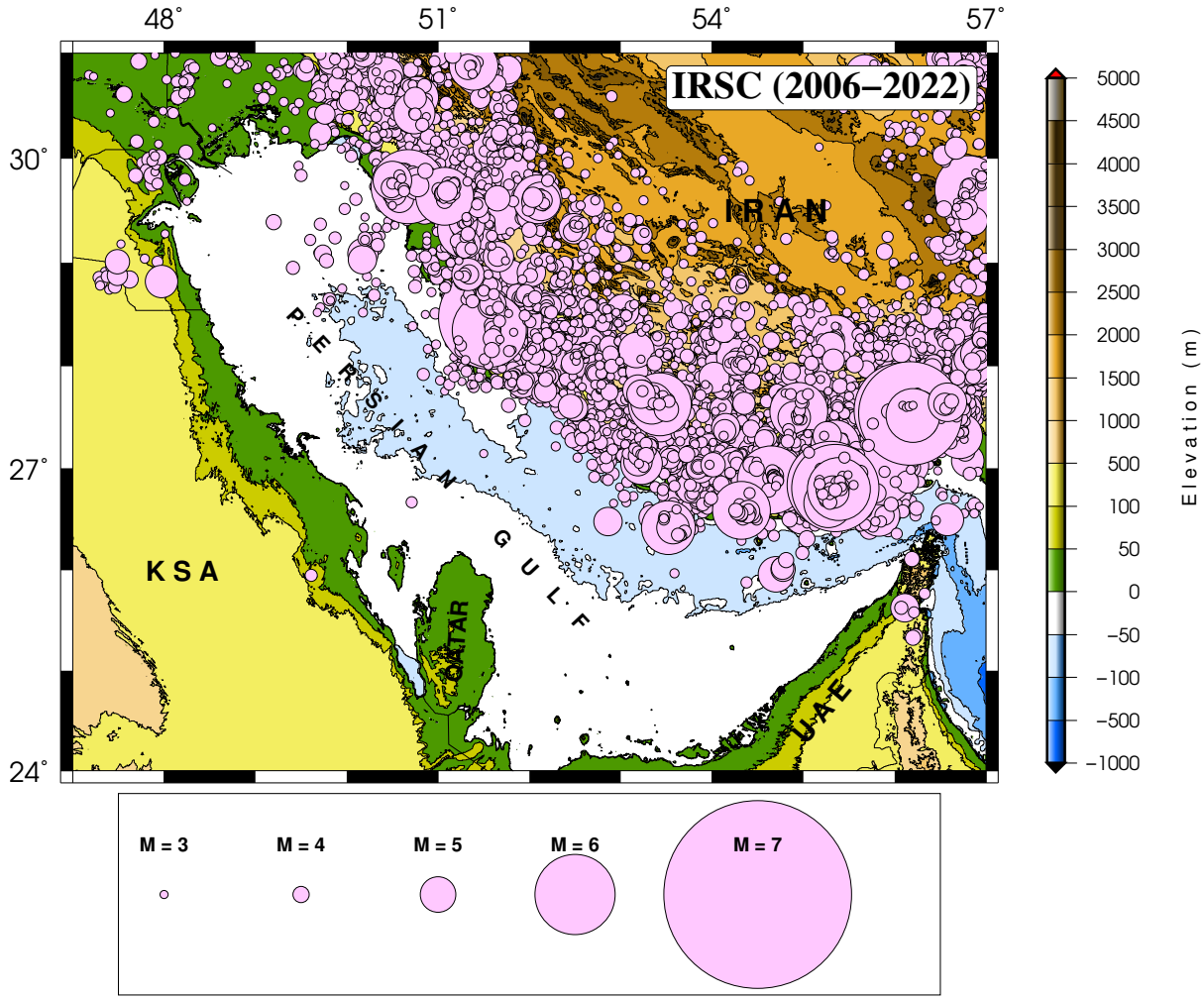

Figure S18: Seismicity of southern Iran and the Persian Gulf from the IRSC catalog. Topography is from Gebco (GEBCO, 2021).

A possible way forward in this regard is to equip the repeaters of existing subsea telecommunication cables with accelerometers. The resulting so-called SMART cables (Howe et al., 2019) will fascillitate the monitoring of offshore events; a process described in detail by Salaree et al. (2022). Fig. S19 shows the location of these cables and their repeaters in the Persian Gulf. However, this process is expensive and requires strategic, long-term planning. There is also considerable distance between the existing seismicity and the positions of these cables in the Persian Gulf. Thus, an alternative, more cost-effective approach in which stations are placed closed to shorelines is desired. HBox can provide this opportnity as shown

in Fig. S20.

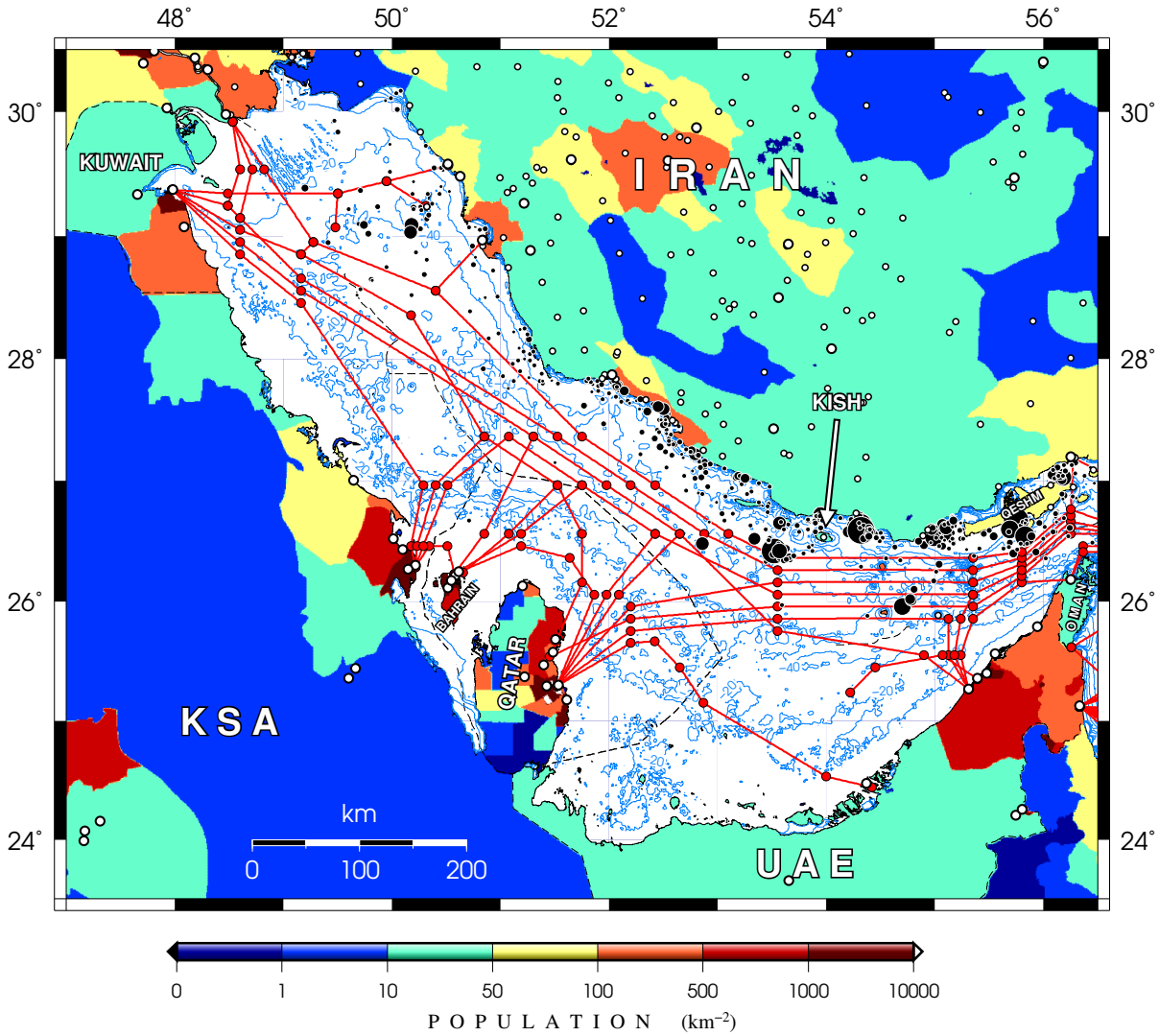

Figure S19: A map of submarine telecommunication cables (red lines) in the Persian Gulf. Red dots show the nominal locations of repeaters. Lands are colored based on population density per square kilometers. White dots depict major cities. Black dots show the locations of offshore seismicity (IRSC) with their sizes proportional to magnitude. White arrow shows the Kish Island.

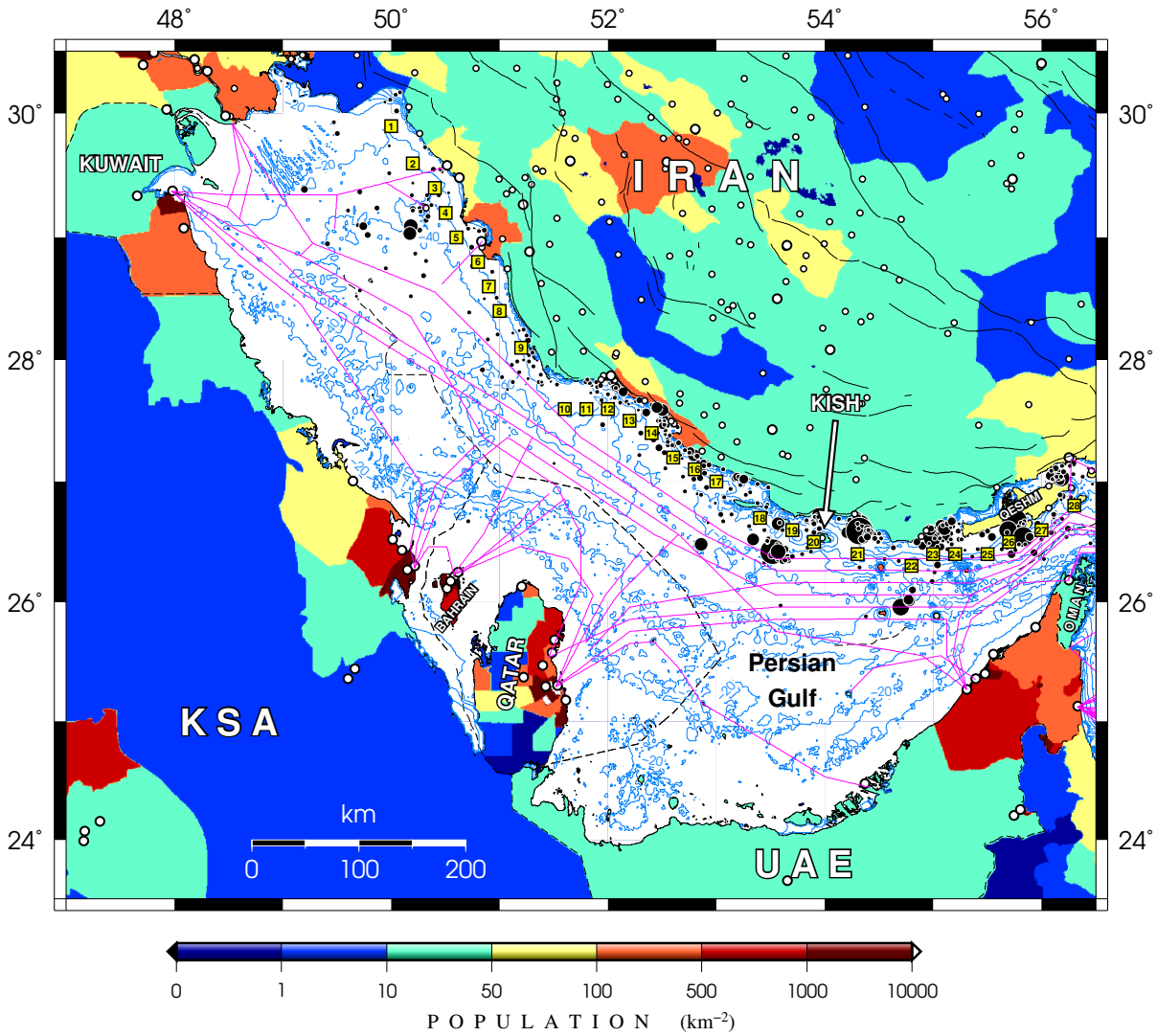

Figure S20: Map of proposed locations for 28 HBox deployments shown as numbered squares. Pink lines are subsea telecommunication cables. All else is identical to Fig. S19.

References

Aki, K. & Richards, P. G., 2002. *Quantitative Seismology*, University Science Books.

Ataie-Ashtiani, B., Rajabi, M. M., & Ketabchi, H., 2013. Inverse modelling for freshwater lens in small islands: Kish Island, Persian Gulf, *Hydrological processes*, **27**(19), 2759–2773.

Berberian, M., 1995. Master "blind" thrust faults hidden under the Zagros folds: Active basement tectonics and surface morphotectonics, *Tectonophysics*, **241**(3-4), 193–224.

BHRC, 2023. Iranian Strong Motion Nework, *Road, Housing & Urban Development Research Center Data Bank*, accessed on 25 Jan 2023.

GEBCO, 2021. Gebco Compilation Group: GEBCO 2021 Grid, *The General Bathymetric Chart of the Oceans*, doi:10.5285/c6612cbe-50b3-0cff-e053-6c86abc09f8f.

Hessami, K., Jamali, F., & Tabassi, H., 2003. Major active faults of Iran, *IIEES, Tehran*.

Howe, B. M., Arbic, B. K., Aucan, J., Barnes, C., Bayliff, N., Becker, N., Butler, R., Doyle, L., Elipot, S., Johnson, G. C., et al., 2019. SMART cables for observing the global ocean: Science and implementation, *Frontiers in Marine Science*, **6**, 424.

Johnson, R. H., Northrop, J., & Eppley, R., 1963. Sources of Pacific T phases, *J Geophys Res*, **68**(14), 4251–4260.

Jong, K. A. D., 1982. Tectonics of the Persian Gulf, Gulf of Oman, and southern Pakistan region, in *Ocean Basin Margin*, pp. 315–351, Springer.

Nedwell, J., Edwards, B., Turnpenny, A., & Gordon, J., 2004. Fish and marine mammal audiograms: A summary of available information, *Subacoustech Report ref: 534R0214*.

Newman, A. V. & Okal, E. A., 1998. Teleseismic estimates of radiated seismic energy: The E/M_0 discriminant for tsunami earthquakes, *J Geophys Res: Solid Earth*, **103**(B11), 26885–26898.

Nissen, E., Tatar, M., Jackson, J. A., & Allen, M. B., 2011. New views on earthquake faulting in the Zagros fold-and-thrust belt of Iran, *Geophys J Int*, **186**(3), 928–944.

Salaree, A. & Huang, Y., 2023. Excitation of back-arc tsunamis from megathrust ruptures: Theory and application to the sea of japan, *Journal of Geophysical Research: Solid Earth*, **128**(2), e2022JB024750.

Salaree, A., Howe, B. M., Huang, Y., Weinstein, S. A., & Sakya, A. E., 2022. A numerical study of SMART cables potential in marine hazard early warning for the Sumatra and Java regions, *Pure Appl Geophys*, pp. 1–33.

Synolakis, C. E., 1999. Exact solutions of the shallow-water wave equations, *Adv Coastal Ocean En*, pp. 61–131.

Vallée, M., Charléty, J., Ferreira, A. M., Delouis, B., & Vergoz, J., 2011. SCARDEC: A new technique for the rapid determination of seismic moment magnitude, focal mechanism and source time functions for large earthquakes using body-wave deconvolution, *Geophys J Int*, **184**(1), 338–358.

Wysession, M. E., Okal, E. A., & Miller, K. L., 1991. Intraplate seismicity of the Pacific Basin, 1913–1988, *Pure and Applied Geophysics*, **135**(2), 261–359.